Inherent structures, fragility, and jamming: Insights from quasi-one-dimensional hard disks

Mahdi Zaeifi Yamchi,[1,*] S. S. Ashwin,[2,†] and Richard K. Bowles[1,‡]
[1]*Department of Chemistry, University of Saskatchewan, Saskatoon, Saskatchewan, Canada S7N 5C9*
[2]*Department of Computational Science and Engineering, Nagoya University, Aichi, Japan*
(Received 30 October 2014; published 3 February 2015)

We study a quasi-one-dimensional system of hard disks confined between hard lines to explore the relationship between the inherent structure landscape, the thermodynamics, and the dynamics of the fluid. The transfer matrix method is used to obtain an exact description of the landscape, equation of state, and provide a mapping of configurations of the equilibrium fluid to their local jammed structures. This allows us to follow how the system samples the landscape as a function of occupied volume fraction ϕ. Configurations of the ideal gas map to the maximum in the distribution of inherent structures, with a jamming volume fraction ϕ_J^*, and sample more dense basins with increasing ϕ. This suggests jammed states with a density below ϕ_J^* are inaccessible from the equilibrium fluid. The configurational entropy of the fluid decreases rapidly at intermediate ϕ before plateauing at a low value and going to zero as the most dense packing is approached. This leads to the appearance of a maximum in both the isobaric heat capacity and the inherent structure pressure. We also show that the system exhibits a crossover from fragile to strong fluid behavior, located at the heat capacity maximum. Structural relaxation in the fragile fluid is shown to be controlled by the presence of high order saddle points caused by neighboring defects that are unstable with respect to jamming and spontaneously rearrange to form a stable local environment. In the strong fluid, the defect concentration is low so that defects do not interact and relaxation occurs through the hopping of isolated defects between stable local packing environments.

DOI: 10.1103/PhysRevE.91.022301 PACS number(s): 64.70.P−, 61.20.Gy, 64.60.De

I. INTRODUCTION

Bernal's [1] construction of random close packing (RCP) using ball bearing hard spheres highlighted the role particle packing may play in understanding the structure of liquids. Subsequent work on jamming phenomena [2–5] has shown that the ways particles pack together to form mechanically stable structures has important implications for the properties of fluids, glasses, and athermal granular materials. In particular, the jamming phase diagram [6–9] was introduced to establish a connection between the jamming in thermal and athermal systems. Packing problems have also found applications in computer science [10] and information theory [11].

The potential energy landscape [12] combined with inherent structures [13,14] provide an ideal framework that connects the properties of the equilibrium fluid with packings of particles by mapping every configuration of the equilibrium fluid to a mechanically stable structure. In a system with potential energy, an inherent structure is a local potential energy minimum obtained by quenching the system using a steepest descent or conjugate gradient energy minimization. In a hard particle system, a configuration is ideally mapped to its inherent structure by continually expanding the particles, moving them apart on contact, until they become collectively jammed [15] in a local maximum density maximum. Configurations that map to the same inherent structure are then grouped together in basins of attraction to form the jamming or packing landscape consisting of local density maxima separated by saddle points. The partition function for the system can then be formed by summing over all the basin volume so that the thermodynamics and dynamics of the system can be described in terms of how the system moves on this high dimensional landscape [16,17]. In particular, shallow basins on the inherent structure landscape have small vibrational volumes, but there are many of them, while deep basins are rare and have large vibrational volumes. As a result, the equilibrium properties of the system are determined by the competition between the configurational (number of basins) and their vibrational entropies so the fluid samples the set of basins that maximizes the total entropy.

The Adam-Gibbs relation [18] suggests the slowdown observed in the dynamics of supercooled fluids is related to the decrease in the number of accessible inherent structure basins N_J through the configurational entropy $S_c/Nk = \ln N_J$. The landscape approach accounts for the possibility of an ideal glass transition to occur if N_J becomes subexponential so that $S_c/N \to 0$. Unfortunately, the inherent structure mapping process for hard particles is difficult to implement for even small numbers of particles [13]. Computer simulation has been used extensively to investigate the distribution of inherent structures, but different compression protocols often lead to different conclusions for both hard disk mixtures [19–21] and hard spheres [7,22]. While the density of RCP is highly reproducible, relationships between structure and the density of jammed packing suggest randomness is ill defined and it has been proposed that it should be replaced by the concept of a maximally jammed state [23]. Similarly, the existence of a continuous distribution of jammed states, from disordered packings through to the ordered crystal, in a binary mixture of hard disks, appears to rule out the possibility of an ideal glass transition [21].

Replica mean field theory [24,25] (RMFT) provides a theoretical approach to understanding jamming in hard particles. The replicated free energy of a dense fluid is parametrized in terms of the local cage size which momentarily traps the

*Mahdi.zaeifi@usask.ca
†ss.ashwin@gmail.com
‡Corresponding author: richard.bowles@usask.ca

particles in the replica space. In order to get relations describing the jammed states, the cage parameter is systematically taken to zero under the resulting mean field constraints. This effectively models the immobilization of a particle due to caging by its local neighbors and suggests there is a very narrow distribution of jammed structures in three-dimensional hard spheres, which is consistent with recent simulations [26–28]. Other theoretical methods include a granocentric model [29] for random packing that focuses on the ability of neighbors to form jamming contacts around a central particle and a recent statistical mechanics approach that accounts for correlations in packings [30].

The goal of this work is study a simple model system for which the complete distribution of inherent structures can be calculated so we can explore the relationships between the properties of resulting landscape and the thermodynamics and dynamics of the fluid. The preliminary results of our analysis appeared in earlier work [31,32] and this paper contains more details and new work regarding the role of defects and soft modes on the dynamics of the fluid. The rest of the paper is organized as follows: Section II introduces the model. Section III describes our analysis of the inherent structure landscape and thermodynamics of the model obtained using the transfer matrix method, while Sec. IV describes the molecular dynamics simulations used to confirm our analytical results and study the dynamics. Our discussion is contained in Sec. V.

II. THE MODEL

The model consists of N two-dimensional (2D) hard disks, with diameter σ, confined between two hard walls (lines) of length L separated by a distance $1 < H_d/\sigma < 1+\sqrt{3/4}$, where H_d is the channel width. The particle-particle and particle-wall interaction potentials are given by

$$V(r_{ij}) = \begin{cases} 0, & r_{ij} \geqslant \sigma \\ \infty, & r_{ij} < \sigma \end{cases} \tag{1}$$

and

$$V_w(r_i) = \begin{cases} 0, & r_y \leqslant |h_0/2| \\ \infty, & \text{otherwise} \end{cases} \tag{2}$$

respectively, where $r_{ij} = \left|\mathbf{r_j} - \mathbf{r_i}\right|$ is the distance between particles, r_y is the component of the position vector for a particle perpendicular to the wall, and $h_0 = H_d - \sigma$ is the reduced channel diameter. The two-dimensional volume accessible to the particle centers is then $h_0 L$ and the occupied volume is $\phi = N\pi\sigma^2/(4LH_d)$.

III. TRANSFER MATRIX METHOD

A. Inherent structure landscape

By confining the disks to a channel width $H_d/\sigma < 1+\sqrt{3/4}$, the particles can only contact their nearest neighbors on each side and the wall. As a result, there are only four local particle configurations that can be combined to form to configurations that satisfy the local jamming constraints in 2D. Figure 1 shows how these can be represented by bonds connecting the centers of neighboring disks. Bonds 1 and 3 represent two dense configurations, while bonds 2 and 4

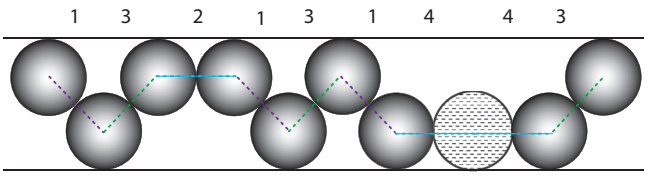

FIG. 1. (Color online) Local packing arrangements of disks. Dashed lines connect the centers of neighboring disks in contact, and the numbers identify different "bonds." Bonds 1 and 3 are the locally most dense states. Bonds 2 and 4 represent the defect states. The $-4-4-$ arrangement results in an unjammed particle (dash filled).

represent open defect type configurations. Bonds 1 and 2 are mirror images of each other, with the mirror plane located along the central axis of the channel. Similarly, bonds 3 and 4 are also mirror images of each other. These bonds can be combined to create locally jammed configurations of N particles that can be described by an ordered list of the bond types. However, not all bond arrangements result in a jammed state because some of the local environments are incompatible with each other. Neighboring $-1-1-$ and $-3-3-$ bonds are incompatible because they start and finish on opposite side of the channel and need to be bridged by a $-3-$ or and $-1-$, respectively, to join particle centers. Configurations of neighboring defects, represented by bonds ($-2-2-$ and $-4-4-$), are also incompatible as they result in a local configuration where the the central disk has three contacts all in the same hemisphere, allowing it to move laterally and unjam. For example, see the gray disk in the $-4-4$ arrangement pictured in Fig. 1. If all the particles in a configuration satisfy the local jamming conditions, then the configuration is also collectively jammed because the particles are unable to pass each other.

We can take advantage of the quasi-one-dimensional nature of our system and use the transfer matrix method to construct the ensemble of inherent structures [33]. The length added to the system along the axis of the channel when a bond of type j follows a bond of type i is l_{ij}, with $l_{i,1} = l_{i,3} = [H_d(2\sigma - H_d)]^{1/2} = \sigma^*$ and $l_{i,2} = l_{i,4} = \sigma$. For fixed N, the volume of the system will fluctuate depending on the number of type 2 and 4 bonds in the configuration so we introduce a longitudinal pressure P, as a conjugate variable to the volume, and fix the system at a constant temperature T. The transfer matrix then takes the form

$$M = \begin{bmatrix} 0 & 0 & M_{1,3} & M_{1,4} \\ M_{2,1} & 0 & 0 & 0 \\ M_{3,1} & M_{3,2} & 0 & 0 \\ 0 & 0 & M_{4,3} & 0 \end{bmatrix}, \tag{3}$$

where $M_{i,j} = C_{i,j}\exp(-\beta P h_0 l_{i,j})$. The exponential term is the Gibbs measure appropriate for the N,P,T ensemble and $C_{i,j}$ is zero when the two bonds are incompatible and one otherwise. In the thermodynamic limit, the partition function for the system is given by

$$\Delta(N,P,T) = NkT\ln(\lambda), \tag{4}$$

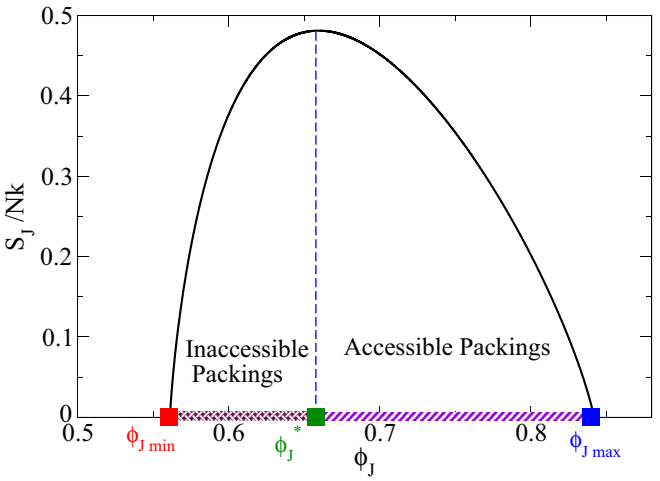

FIG. 2. (Color online) S_J/Nk versus ϕ_J for $H_d/\sigma = 1.866$. The thermodynamically accessible packings have occupied volume fractions between $\phi_J^* = 0.659$ (green square) and the most dense jammed state $\phi_{J\,\max} = 0.842$ (blue square). The thermodynamically inaccessible exist below ϕ_J^* and the least dense state $\phi_{J\,\min} = 0.561$ (red square).

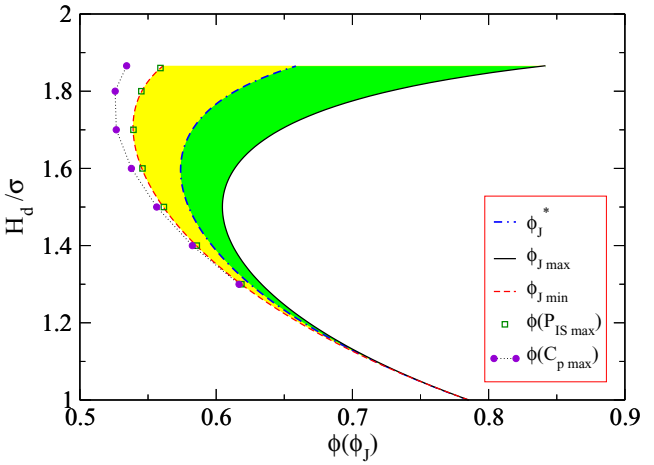

FIG. 3. (Color online) The jamming phase diagram showing $\phi_{J\,\max}$, $\phi_{J\,\min}$, and ϕ_J^* as a function of H_d/σ. The ϕ of the maxima for the inherent structure pressure P_{IS} and the heat capacity C_p are included for comparison. The green (dark gray) area identifies the accessible jammed packings and the yellow (light gray) area represents the inaccessible jammed packings.

where λ is the largest eigenvalue of M. The jamming density ϕ_J is then given by

$$\phi_J = \frac{N\pi\sigma^2}{4H_d L_J} = -\frac{\pi\sigma^2}{4kT\,H_d\partial\,(\ln\lambda)\,/\partial P}, \tag{5}$$

where L_J is the length of the system in the jammed state. The entropy of jammed states $S_J = k\ln N_J$, where N_J is the number of jammed configurations with ϕ_J, can be written as

$$S_J/Nk = \ln\lambda + T\partial\,(\ln\lambda)\,/\partial T. \tag{6}$$

The resulting eigenvalues are necessarily functions of N, P, and T. The factors associated with N are dealt with by considering the system in the thermodynamic limit and calculating quantities on a per particle basis. T plays no direct role in the hard particle system, except to provide the velocity distribution of the particles. Here, we are only dealing with jammed structures where there is no free volume and the particles are unable to move, which implies that $T = 0$. The equilibrium fluid, including free volume, is described in Sec. III B. In the absence of temperature, there is no internal pressure caused by the collision between particles. However, it is still necessary for the system to do work against the pressure P when it expands so the equation of state for the ensemble of jammed configurations results from the connection between the work required to expand the volume of the system and S_J. We obtain the full distribution of states by varying the pressure from $-\infty \to \infty$.

Figure 2 shows that the distribution of jammed states has a similar form to that obtained for the one-dimensional (1D) model [34], but with a lower entropy because of the need to eliminate states with neighboring defects. The results obtained using the transfer matrix method are identical to those obtained using a combinatorial approach, which gives [35]

$$\phi_J = \frac{\pi}{4H_d[\theta + (1-\theta)\sqrt{H_d(2-H_d)}]}, \tag{7}$$

and

$$S_J/Nk = (1-\theta)\ln(1-\theta) - \theta\ln\theta - (1-2\theta)\ln(1-2\theta), \tag{8}$$

where θ is the fraction of defect bonds (2 and 4). The most dense and least dense states occur when $\theta = 0$ and 0.5, respectively, and both have $S_J = 0$. The most dense state is obtained in the limit $P \to \infty$ and the least dense state is obtained as $P \to -\infty$. The density distribution of inherent structures goes through a maximum at an intermediate density, ϕ_J^* when $\theta = 1/2 - \sqrt{5}/10$ and $P = 0$. The jamming phase diagram for the model (Fig. 3) shows that while the functional form of the distribution of inherent structures remains the same over the range of channel diameters $1 \leqslant H_d/\sigma \leqslant 1 + \sqrt{3/4}$, the width of the distribution collapses to a single state, in the limit $H_d/\sigma \to 1$, when the system effectively becomes one dimensional. The distribution broadens as H_d increases, but $\phi_{J\,\max}$ and $\phi_{J\,\min}$ go through minima due to the varying lengths l_{i1} and l_{i3}. The range of jammed states from $\phi_{J\,\max} - \phi_{J\,\min}$ represents the J line.

It is also notable that the low density jammed states (large volume) were obtained under conditions of negative pressure. This is purely a consequence of the thermodynamic relation $P = T(\partial S/\partial V)_U$ and that the number of low density jammed states is decreasing as the volume of the packings increases. In many respects, it is similar to the appearance of negative temperatures in systems with upper energy bounds. However, negative pressures cannot actually be realized because there are no attractive forces in the hard sphere system to balance the tension. We will see in the next section that the equilibrium fluid, which exists from the ideal gas in the low ϕ limit, up to the most dense jammed state $\phi_{J\,\max}$, only samples inherent structures above the maximum in the ϕ_J distribution so that the "negative pressure" states are never sampled, making them inaccessible.

In the context of understanding athermal granular systems, a knowledge of the ensemble of jammed states is of considerable

interest to the development of a granular statistical mechanics [36], and the current model has been used to test ideas relating to temperaturelike thermodynamic quantities such as the compactivity [37–40].

B. Thermodynamics of the equilibrium fluid

The goal of this section is to investigate how the thermodynamics of the equilibrium fluid relates to the underlying inherent structure landscape. Barker [41] originally provided an exact solution for the partition function of quasi-one-dimensional systems. Kofke *et al.* [42] then developed a transfer matrix method for solving the partition function of a system of hard particles in a channel, where second nearest neighbor interactions are excluded. In this approach, the y positions of the particles are fixed and a liquid configuration is mapped to a configuration of tangent disks, by translating the disks along the x axis, so the system becomes a 1D mixture of additive hard rods with different contact lengths. This allows the integration over the x coordinates of the particles to be performed independently of the integration of the y coordinates. The solution to the partition function can then be represented as an eigenvalue problem where the largest eigenvalue is used in the thermodynamic limit. The partition function in the N,P,T ensemble can be written as a transfer integral

$$Z = \frac{1}{\Lambda^{DN}(\beta P)^{N+1}} \int dy\, K^N(y_1,y_2). \tag{9}$$

Here, Λ is the thermal wavelength, P is the longitudinal pressure, and the kernel K is defined as

$$K(y_1,y_2) = \exp[-\beta P h_0 L_x(y_1,y_2)], \tag{10}$$

with y_1 and y_2 being the y coordinates of two adjacent disks in contact. L_x is the projection of the distance between the two contacting disks along the x axis and is a function of y_1, y_2. In principle, $K(y_1,y_2)$ is an infinite dimensional matrix because y_1 and y_2 are continuous variables, but we are interested in the largest eigenvalue λ, which satisfies

$$\int dy\, K(y_1,y)\,\psi(y) = \lambda\psi(y_1), \tag{11}$$

where ψ is an eigenfunction. The eigenvalue problem is solved by using a mesh for the y coordinates [42]. The molar Gibbs free energy g is then given by

$$\beta g = \ln\Lambda + \ln(\beta P) - \ln(\lambda), \tag{12}$$

and this can be used to obtain the equation of state.

The properties of the equilibrium fluid are obtained by maximizing the total entropy of the system at a given density, which requires a balance between the configurational entropy, i.e., the number of basins sampled at ϕ with a given ϕ_J, and the vibrational entropy of those basins. To determine which inherent structures are sampled by the equilibrium fluid as a function of density, we take advantage of the information contained within the matrix K regarding the geometry of adjacent tangent disks. Our compression scheme is summarized in Fig. 4. Starting from an equilibrium configuration, the particles are compressed along the x axis, with fixed y coordinates, until all the disks are in contact. Figure 4 then

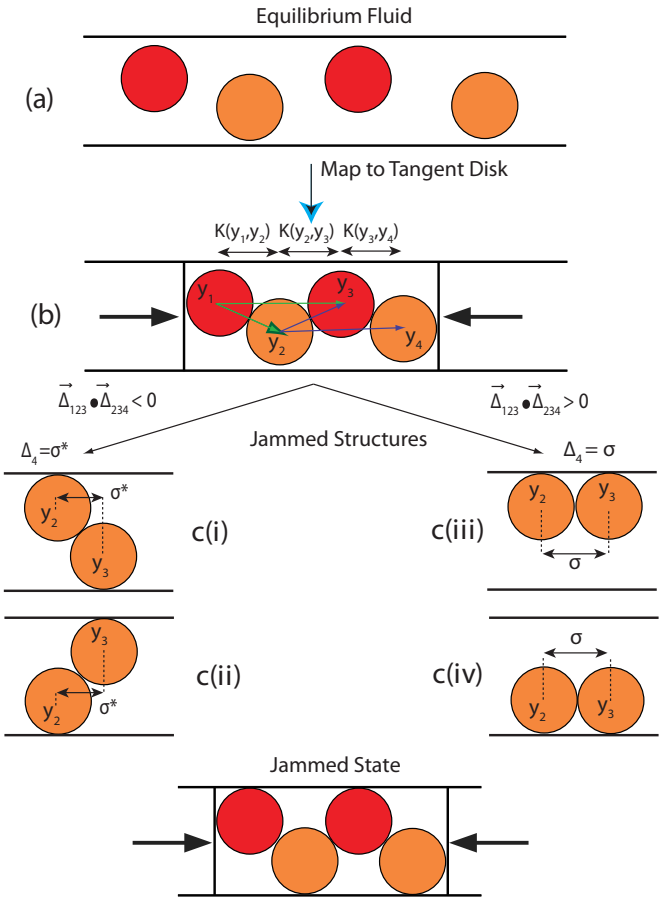

FIG. 4. (Color online) In order to map equilibrium fluid configurations to the jammed configurations analytically, we introduce a matrix G_4 using a group of four disks. Disks 1, 2, 3, 4, in a liquid configuration (a) are mapped to a set of tangent disks (b). The product of the kernels $K(y_1,y_2)K(y_2,y_3)K(y_3,y_4)$ is then constructed. Squeezing disks 1 and 4 towards each other determines the jamming configuration of disks 2 and 3. Δ_4 is the projection of the distance between disks 2 and 3 along the x axis, in the jammed configuration. Δ_4 is either σ or σ^* depending on the rules c(i) and c(ii) or c(iii) and c(iv), respectively. The product kernel is then weighed with Δ_4 to give the G_4 matrix.

shows that the type of bond formed between the two central disks (2,3) as the result of further compression. This can be determined from the sign of the product of areas made from the triangles created by particles 1, 2, 3 and 2, 3, 4. The geometry of the four disks is contained in the chain product matrix $K(y_1,y_2)\,K(y_2,y_3)\,K(y_3,y_4)$. The product *area-vector-product* rule, for triangles $\vec{\Delta}_{123}$ and $\vec{\Delta}_{234}$, that determine the nature of the bonds is

$$\begin{aligned} \vec{\Delta}_{123}\cdot\vec{\Delta}_{234} > 0 \quad \text{bond 2,3} \quad \Delta_4 = \sigma^*, \\ \vec{\Delta}_{123}\cdot\vec{\Delta}_{234} < 0 \quad \text{bond 2,3} \quad \Delta_4 = \sigma. \end{aligned} \tag{13}$$

We can now define a new, four particle transfer matrix

$$G_4(y_1,y_4) = \int K(y_1,y_2)K(y_2,y_3)K(y_3,y_4)\exp[\gamma\Delta_4]dy_2dy_3 \tag{14}$$

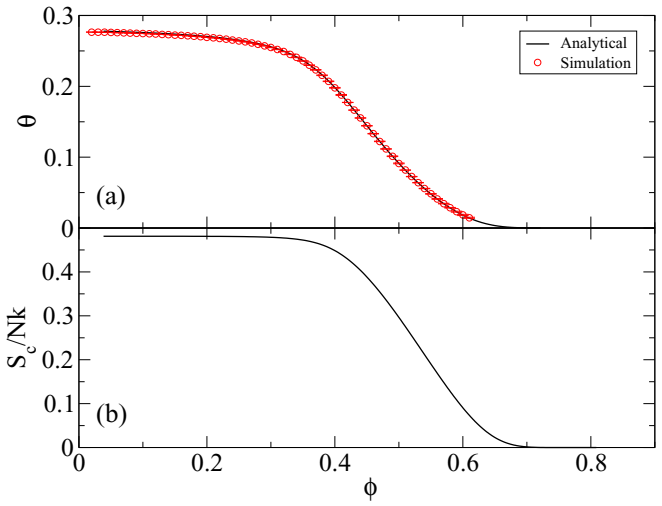

FIG. 5. (Color online) (a) The fraction of defect bonds in the inherent structures sampled by equilibrium fluid at ϕ. The solid line represents the transfer matrix results and the open circles were obtained from simulation (see Sec. IV A). (b) The configurational entropy of the equilibrium fluid.

whose elements are weighted by the bonds they would form when jammed. For a system with periodic boundary conditions and $N-2$ particles, the volume of the inherent structure formed when the equilibrium fluid is at P is given by

$$V_{2N}^{inh} = \lim_{\gamma\to 0} \partial \ln[\mathrm{Tr}(G_4)]/\partial\gamma. \tag{15}$$

The same approach can be used to obtain the fraction of defects in the inherent structure sampled by the fluid $\theta(\phi)$ by setting Δ_4 equal to 1 and 0 for the defect states and dense states, respectively, and then using Eq. (15). The configurational entropy $S_c(\phi)$ is a property of the equilibrium fluid and is given by the number of basins sampled at ϕ. To obtain S_c the equilibrium fluid $\theta(\phi)$ is used in the expression for S_J given by Eq. (8). Figure 5 shows both θ [Fig. 5(a)] and S_c [Fig. 5(b)] as a function of ϕ for a system with $H_d/\sigma = 1.866$. In particular, we see that the ideal gas samples the inherent structures at the maximum of the distribution ϕ_J^*, then the fluid moves to basins with a higher ϕ_J with increasing density. The basins with $\phi_J < \phi_J^*$ are never sampled by the equilibrium fluid. At low ϕ, the configurational entropy of the fluid decreases slowly before it begins a rapid decrease at intermediate occupied volume fractions. An extrapolation of the S_c to higher ϕ, based on its behavior in this intermediate regime, would suggest the system exhibits a Kauzmann catastrophe where the configurational entropy goes to zero at a ϕ well below $\phi_{J\,\max}$. However, at high densities, there are very few basins (although not subexponential) and the vibrational entropy of the basins dominates the properties. This causes S_c/Nk to plateau at high ϕ so that it only approaches zero in the limit $\phi \to \phi_{J\,\max}$. As a result, there is no ideal glass transition in this system.

There is considerable evidence to suggest that the higher order saddle points, connecting the basins of the stable states, also play an important role in the dynamics and structural relaxation of the supercooled fluids [43,44]. In a system with potential energy, saddle points can be classified on the basis of the number of negative eigenvalues in the Hessian matrix of the potential energy of the configuration. When there are no negative eigenvalues, the saddle point is a stable inherent structure, otherwise the system contains one or more unstable, "soft" modes. A statistical measure of these saddle points is captured by the saddle point index, which is the average number of negative eigenvalues in the liquid [45,46]. The saddle point index has been shown to decrease with temperature below the onset temperature for the Kob-Andersen binary Lennard-Jones mixture (KA BLJM) [47], and go to zero at a finite temperature T_d, very close to the mode coupling critical temperature. A crossover from fragile to strong liquid behavior also occurs at T_d [48] in the KA BMLJ model.

The Hessian matrix cannot be calculated in a hard particle system. However, we can identify the local unstable modes in our model as those associated with neighboring defects, i.e., with $-1-4-4-3-$ and $-3-2-2-1$ bond configurations. Building on our method for mapping configurations to their local inherent structures, we can use the transfer matrix approach to map clusters of five disks to their local structure and calculate the probability of finding the unstable states. A configuration of five disks is initially compressed in along the x axis, with y coordinates held fixed, until all the disks are in contact with their neighbors. The unstable states are then identified using the triangle rules for neighboring particles to define Δ_5 as

$$\begin{aligned}
&\vec{\Delta}_{123}\cdot\vec{\Delta}_{234} < 0 \quad \vec{\Delta}_{234}\cdot\vec{\Delta}_{345} < 0 \Rightarrow \Delta_5 = 1,\\
&\vec{\Delta}_{123}\cdot\vec{\Delta}_{234} > 0 \quad \vec{\Delta}_{234}\cdot\vec{\Delta}_{345} < 0 \Rightarrow \Delta_5 = 0,\\
&\vec{\Delta}_{123}\cdot\vec{\Delta}_{234} < 0 \quad \vec{\Delta}_{234}\cdot\vec{\Delta}_{345} > 0 \Rightarrow \Delta_5 = 0,\\
&\vec{\Delta}_{123}\cdot\vec{\Delta}_{234} > 0 \quad \vec{\Delta}_{234}\cdot\vec{\Delta}_{345} > 0 \Rightarrow \Delta_5 = 0.
\end{aligned} \tag{16}$$

Once the five particle transfer matrix is defined,

$$G_5(y_1,y_5) = \int K(y_1,y_2)K(y_2,y_3)K(y_3,y_4)K(y_4,y_5) \times \exp[\omega\Delta_5]\prod_{i=2}^{4} dy_i, \tag{17}$$

the fraction of configuration space associated with the unstable states ($\Delta_5 = 1$) is given by

$$\eta = \lim_{\omega\to 0} \partial[\ln \mathrm{Tr}(G_5)]/\partial\omega. \tag{18}$$

RMFT identifies ϕ_d as the occupied volume fraction where long lasting glassy states first appear, causing the dynamics to become activated. In the bulk, three-dimensional hard sphere system $\phi_d \sim 0.58$, which coincides with the mode coupling transition. Godfrey and Moore [49] found the correlation length for the confined disks model increased rapidly at intermediate ϕ and would appear to diverge near $\phi = \phi_d \sim 0.48$ based on an extrapolation. However, the transition is avoided and the growth of the correlation length slows down at higher ϕ. Figure 6 shows that our analysis of η essentially follows that of the inverse correlation length obtained by Godfrey and Moore, decreasing rapidly before plateauing at very low values ($\eta \sim 0$). A linear extrapolation from lower ϕ would locate $\phi_d \sim 0.5$. This suggests a change in the nature of

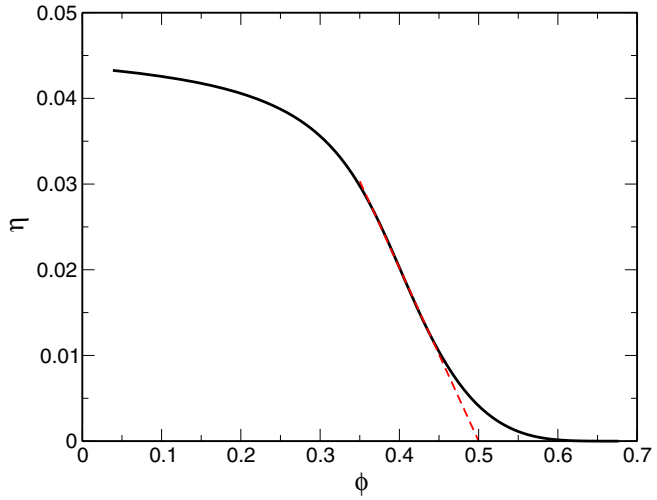

FIG. 6. (Color online) η as a function of ϕ. The solid line represents data calculated using the transfer matrix. The dashed (red) line is the linear extrapolation.

the dynamics may occur when defects become rare, such that they do not interact to produce soft modes. In principle, we should also include an analysis of higher order saddle points that include $-2-2-2$ and $-2-2-2-2-$ states, etc., but these are even more rare and their inclusion would not change the qualitative features described here.

The isobaric heat capacity is $C_p = (\partial H/\partial T)_P$. For hard disks, the enthalpy is $H = NkT + PV$ and

$$C_p/Nk = 1 + Z/(1 + d\ln\{Z\}/d\ln\{\phi\}), \tag{19}$$

where $Z = PV/NkT$ and V is the thermodynamic volume accessible to the centers of the particles. Figure 7(a) shows that the fluid exhibits a maximum in the heat capacity that sharpens and moves to lower T as the distribution of inherent structures narrows with decreasing H_d, before collapsing to

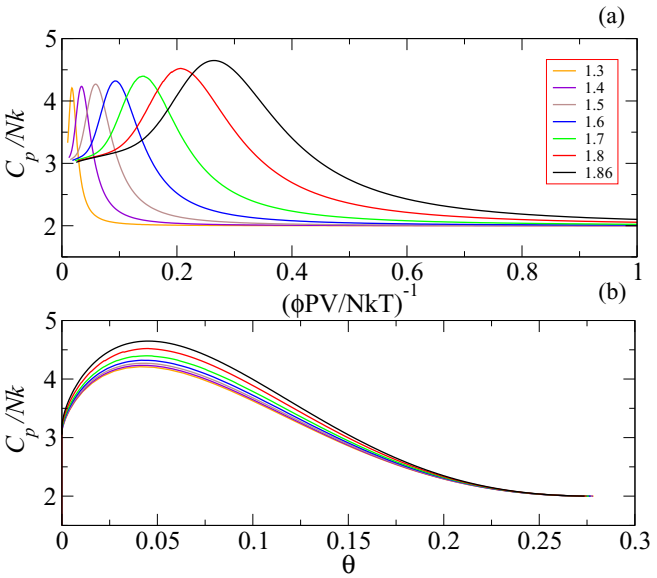

FIG. 7. (Color online) C_p/Nk as a function of $(\phi PV/NkT)^{-1}$ (top) and defect fraction θ (bottom).

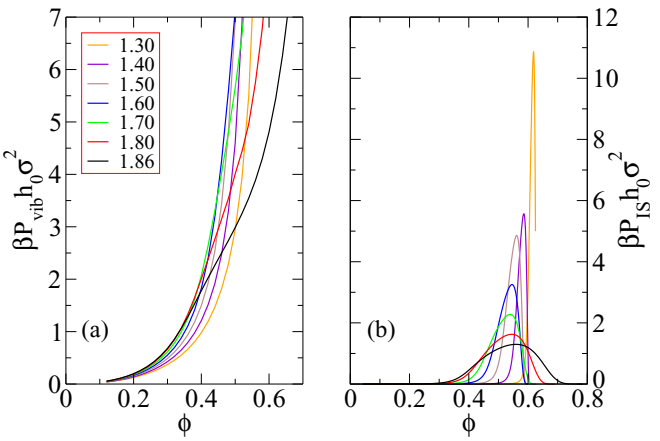

FIG. 8. (Color online) Vibrational pressure and inherent structure pressure versus ϕ for different values of H_d/σ.

a single structure at $H_d/\sigma = 1$. For the system with $H_d/\sigma = 1.866$, the maximum is located at $\phi = 0.534$, which is only just above ϕ_d. If C_p is replotted as a function of the equilibrium number of defects in the fluid [see Fig. 7(b)], we see that the maximum occurs at the same value $\theta = 0.044 \pm 0.002$ for all H_d, suggesting the concentration of defects is the key feature controlling the behavior of the heat capacity maximum.

Shell and Debenedetti [50] showed that the properties of the equation of state (EOS) of a fluid could be related to the inherent structure landscape by separating the equilibrium pressure into contributions from the inherent structure pressure P_{IS} and the vibrational pressure $P_{\rm vib}$, so that

$$P = (P_{IS} + P_{\rm vib}). \tag{20}$$

Making use of the general relation $P = T(\partial S/\partial V)_U$, we can calculate the inherent structure pressure as

$$\beta P_{IS} h_0 \sigma^2 = -\frac{4H_d\phi^2}{\pi}\left(\frac{\partial S_c/Nk}{\partial\phi}\right)_U, \tag{21}$$

and then obtain $P_{\rm vib}$ from Eq. (20). Both contributions to the pressure are shown in Fig. 8. The vibrational pressure increases monotonically as a function of ϕ while P_{IS} exhibits a maximum at densities that are slightly higher than the where the C_P maximum appears. The location of the maxima in the heat capacity and the inherent structure pressure have been included on the jamming phase diagram for the model (Fig. 3).

IV. MOLECULAR DYNAMICS SIMULATIONS

A. Exploring the packing landscape

In this section, we describe a series of event driven molecular dynamics simulations carried out in the canonical (N,V,T) ensemble. They help verify our transfer matrix analysis and provide measurements of dynamic properties of the system. $N = 10^4$ particles were initially placed in a linear lattice at $\phi = 0.01$, and were assigned random velocities that were then scaled to ensure $kT = 1$. The units of time in the simulation are $\sigma\sqrt{m/kT}$, where m is the mass of the particles, which was taken to be unity. At each density studied, the system was equilibrated for $200N - 10^6N$ collisions before

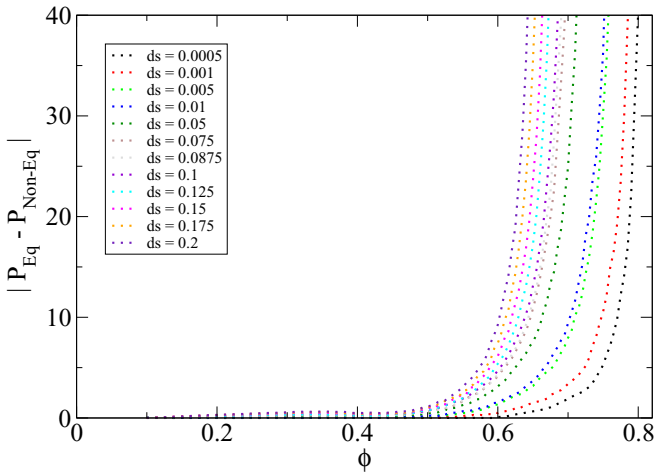

FIG. 9. (Color online) The difference between the equilibrium EOS and the nonequilibrium EOS as a function of ϕ, with $H_d/\sigma = 1.866$, for different compression rates.

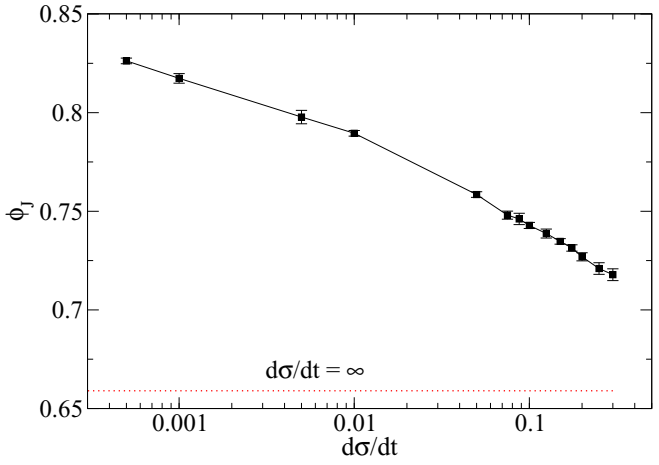

FIG. 10. (Color online) ϕ_J as a function of $\partial\sigma/\partial t$ for a system with $H_d/\sigma = 1.866$. The solid line joins points to provide a guide. The dashed line represents the ϕ_J obtained for the ideal gas using the transfer matrix method.

sampling over the next $400N - 10^7N$ collisions, with the longer run times being used at high densities. A modified version of the Lubachevsky and Stillinger [51] (LS) algorithm, that ensures H_d/σ remains constant as the diameter of the disks is changed (L fixed), was used to compress the system to higher occupied volume fractions, with a compression rate of $d\sigma/dt = 0.001$. The EOS obtained from our simulations matches the exact result within simulation error up to very high occupied volume fractions where we finally fall out of equilibrium at the longest time scales used in our simulations. This occurred near $\phi \sim 0.8$ with $H_d/\sigma = 1.866$.

To follow how the equilibrium liquid moves through the packing landscape as a function of ϕ and compare our simulations with our transfer matrix inherent structure mapping, we measure the defect concentration in the fluid using the triangular method introduced by Speedy [19]. In this method, the position of each disk is considered relative to its two neighbors. If the central disk is located below the line connecting its two neighbors, it will pack at the bottom of the channel, otherwise it will pack at the top. The configuration is then assigned bond numbers, equivalent to those described in Fig. 1, allowing us to identify defects in liquid state without having to compress the system to a jammed state. Figure 5 shows that the defect concentration obtained in our simulations is the same as that obtained using the transfer matrix inherent structure mapping.

Our MD simulations also allow us to explore how the fluid falls out of equilibrium by following the nonequilibrium EOS of the fluid as it is continually compressed. The simulations started at $\phi = 0.05$ and the system was compressed to its jammed configuration using the LS method, with different compression rates in the range $d\sigma/dt = 0.0005$–0.3. The nonequilibrium pressure, at a given density, was obtained by measuring the sphere-sphere and sphere-wall momentum transfer over $10N$ collisions, as the system was still being compressed. Figure 9 shows the difference between the nonequilibrium EOS and the equilibrium EOS obtained from the transfer matrix method. At low ϕ, the nonequilibrium EOS essentially follows that of the equilibrium system because the motion of the particles allows it to move between basins and relax as the fluid is compressed. The small positive differences result from the continual increase in ϕ as the pressure measurement is made, and this occurs more rapidly at faster compression rates. At the fastest compression rates considered here, the system falls out of equilibrium at $\phi \sim 0.5$, as the nonequilibrium EOS begins to diverge, leading to a jammed state with $\phi_J \sim 0.72$ (see Fig. 10). It is interesting to note that the system first shows signs of falling out of equilibrium at a ϕ close to the ϕ_d identified using the saddle point index. As the compression rate is decreased, the fluid remains in equilibrium longer and becomes trapped in a glass with a higher ϕ_J. In principle, if the system was compressed infinitely slowly, it would remain in equilibrium and become jammed at $\phi_{J\,\max}$. Furthermore, Godfrey and Moore [49] were able to predict the compression rate dependence of ϕ_J on the basis of a transition state theory that estimates the time for two defects to diffuse together and annihilate each other through one of the unstable saddle points. Once the rate of compression is faster than that of the rate of annihilation, the total number of defects becomes fixed and the system falls out of equilibrium. The transition state theory was also able to predict the time associated with particles hopping in defects obtained from molecular dynamics simulations [35].

B. Relaxation times

To study the relationship between the packing landscape and the dynamics of the fluid, we calculated the structural relaxation times for the system over a range of ϕ, using two different methods. All simulations used $N = 2000$ particles. Starting from $\phi = 0.01$, between $400N$–10^6N collisions were used to reach equilibrium, then relaxation times were measured with simulation lengths that varied from $200N$ up to 10^6N, depending on the occupied volume fraction. 8×10^4 equally spaced configurations were sampled at each ϕ.

We began by measuring the relaxation time defined in terms of the intermediate scattering function. The longitudinal

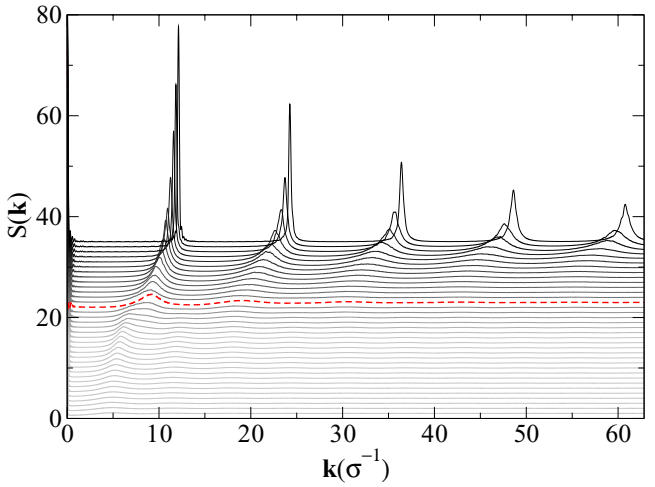

FIG. 11. (Color online) Structure factor $S(\mathbf{k})$ as a function of $\mathbf{k}$ (in units of inverse σ), for all ϕ investigated with $H_d/\sigma = 1.866$. For clarity, the individual curves have been displaced vertically by 1 with increasing ϕ. The dashed (red) curve highlights the data for $\phi = 0.534$, corresponding to the ϕ of the C_p maximum.

structure factor for the system can be defined as

$$S(\mathbf{k}) = \frac{1}{N}\langle \rho_{\mathbf{k}}\rho_{-\mathbf{k}}\rangle, \tag{22}$$

where

$$\rho_{\mathbf{k}} = \sum_{j=1}^{N} \exp[-i\mathbf{k}\cdot\mathbf{r}_{xj}(t)], \tag{23}$$

$\mathbf{r}_{xj}$ is the position of particle j along the x coordinate, at time t, and the angular brackets denote an equilibrium ensemble average over multiple configurations at different t. The wave vector $\mathbf{k}$ was defined along the x axis, as $\mathbf{k} = 2\pi n/L_x$ and the integers n were chosen in the range 1–60. Figure 11 shows the evolution of $S(\mathbf{k})$ as a function of ϕ. The emergence of the first peak, at small $\mathbf{k}$, reflects the growth in real space of the regular zigzag arrangements of the particles associated with the most dense packing. In particular, we see a rapid, but still continuous, shift of the peak to larger $\mathbf{k}$ at ϕ near the C_p maximum. Significant structural changes from a fluidlike to a solidlike structure have also been observed in the pair correlation function at these ϕ [52,53].

The structural relaxation time for the system was then obtained by measuring the self part of the intermediate scattering function

$$F_s(\mathbf{k},t) = \frac{1}{N}\langle \rho_{\mathbf{k}}(t)\rho_{-\mathbf{k}}(0)\rangle \tag{24}$$

at the wave vector $\mathbf{k}_{\max}$, corresponding to the peak of the first maximum in S($\mathbf{k}$). Figure 12(a) shows that the decay of $F(\mathbf{k}_{\max},t)$ reaches zero in the time scale of the simulation, suggesting the system behaves like an equilibrium fluid for all ϕ studied. The structural relaxation time τ_F was then defined as the time required for $F(\mathbf{k}_{\max},t)$ to fall to e^{-1} of its initial value. For a hard particle system, ϕPV is a constant along an isobar and the Arrhenius law would predict that $\ln \tau_F$ varies linearly with $\phi PV/NkT$. Figure 13 shows τ_F is close to being

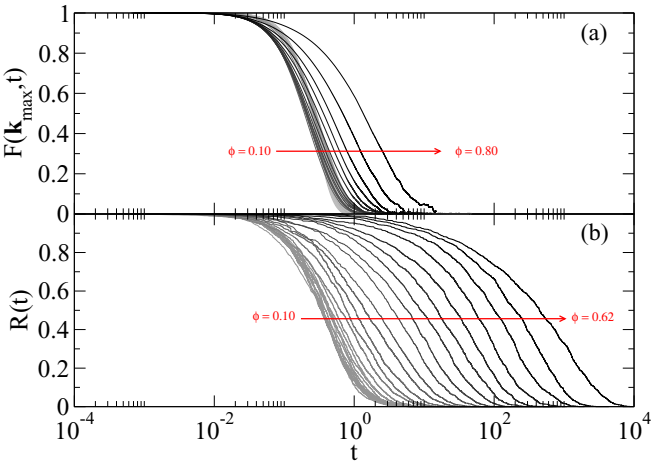

FIG. 12. (Color online) The time dependence of (a) the self-intermediate structure factor $F(\mathbf{k}_{\max},t)$ and (b) the bond survival probability $R(t)$ for a system with $H_d/\sigma = 1.866$, over a range of ϕ.

linear in $1/T$, at high ϕ, which is the behavior expected for a strong fluid, but at lower ϕ, the temperature dependence becomes less clear. In particular, with $H_d/\sigma = 1.866$, we see an unusual decrease in the relaxation times. This may be caused by the rapid structural evolution of the system at these ϕ and is complicated by the corresponding variation of $\mathbf{k}_{\max}$.

As an alternative, we also measured a relaxation time based on the the survival probability of the bond types used to describe the local packing in the inherent structures. At $t = 0$, Speedy's triangular method, described earlier, was used to identify the local bond types throughout the configuration. The fluid remains within the basin of a single inherent structure for a short time before a local rearrangement of the disks changes the identity of some of the bonds and moves the system to a new inherent structure. We measured $R(t)$, the fraction of bonds that have not changed at least once in time t as a function of t, and define the relaxation time as

$$\tau = \int_0^\infty R(t)\,dt. \tag{25}$$

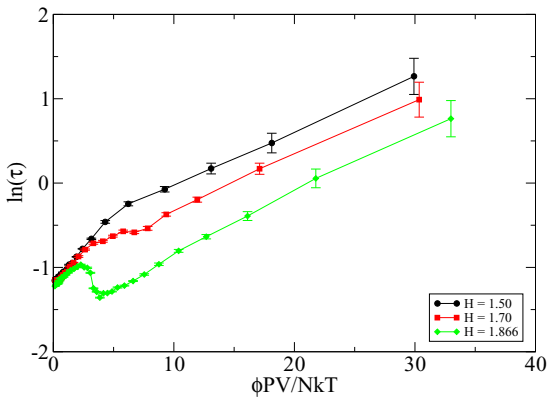

FIG. 13. (Color online) Arrhenius plot for the relaxation times obtained from self-intermediate function for different values of H_d/σ.

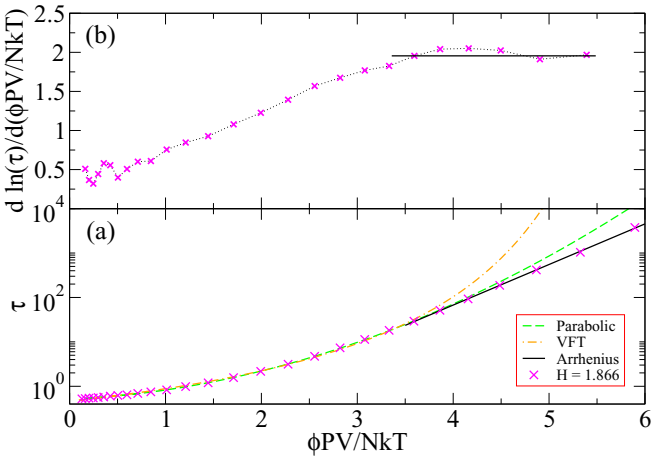

FIG. 14. (Color online) (a) The Arrhenius plot of τ fora system with $H_d/\sigma = 1.866$. The crosses represent the simulation data. The dashed and dashed-dotted lines represent fits to the data in the fragile region of the parabolic and VFT equations, respectively. The solid line is the Arrhenius fit to the strong fluid region. (b) The fragility parameter m calculated from the simulation data. The solid line denotes the slope from the Arrhenius behavior fit to the τ data shown in (a).

$R(t)$ decays in the same fashion as $F(\mathbf{k}_{\max},t)$ [see Fig. 12(b)], but τ is well behaved over the full range of ϕ studied [see Fig. 14(a)]. The linear behavior in $1/T$ at high ϕ remains, but we now see the fluid exhibits a super-Arrhenius behavior at low ϕ, suggesting the system has a fragile-strong fluid crossover. We also show fits of the data from the fragile region to the Vogel-Fulcher-Tammann (VFT) equation [54–56], which predicts a divergence of the relaxation times at a temperature $T_{\rm VFT} > 0$ K, along with the parabolic law developed by Elmatad, Chandler, and Garrahan [57,58], which predicts no singularity and is derived on the basis of the facilitated dynamics model [59]. Both equations fit well when restricted to the fragile fluid data (as shown), but the fits become worse when extended over a full range of data. The Arrhenius equation provides the best fit for τ above the crossover. Good fits of the VFT equation to a wide range of experimental and simulation data for supercooled liquids have been used as evidence for the presence of a thermodynamic singularity underlying the experimentally observed glass transition. However, we have already shown that our model does not exhibit an ideal glass transition, which suggests that $T_{\rm VFT}$ is simply a fit parameter with no physical significance.

To further confirm the existence of the fragile-strong crossover, we also calculate the fragility parameter [60]

$$m = \left(\frac{d \ln \tau}{d\left(\frac{1}{T}\right)} \right), \tag{26}$$

where the derivatives were obtained directly from our data points, without any curve fitting, using a centered differences scheme. Figure 14(b) shows m increases linearly at high temperatures but then plateaus to a constant value when the fluid becomes strong. The crossover point occurs at the C_p maximum.

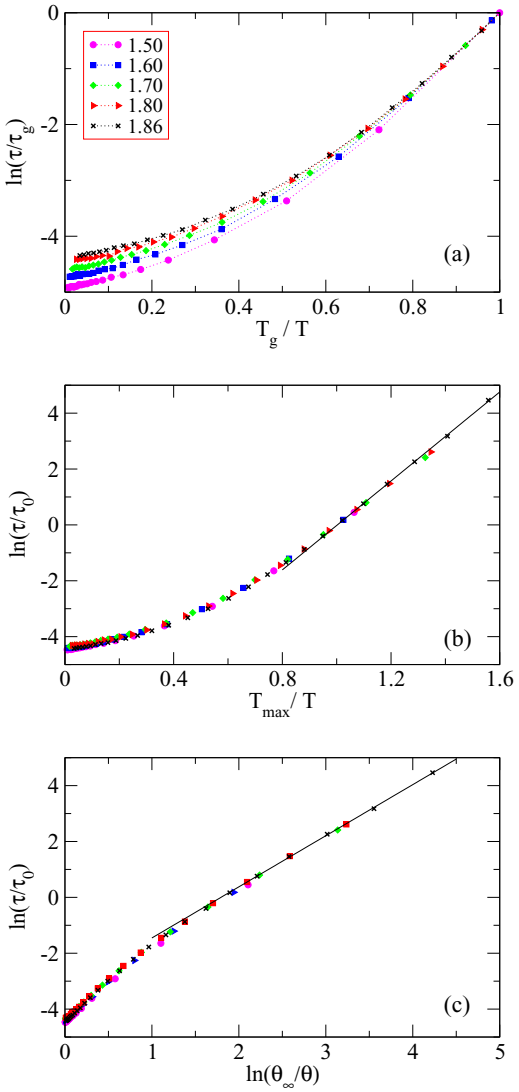

FIG. 15. (Color online) Structural relaxation times for different H_d/σ rescaled by (a) the "glass transition" time and temperature (see text for definition), (b) the time and temperature of the C_p maximum, and (c) the defect concentration relative to the defect concentration in the ideal gas θ_∞.

A comparison of the glass forming properties of different systems is usually achieved by the rescaling of the temperature of the system by the glass transition temperature T_g, which is defined as the temperature where the relaxation time of the system reaches a given value τ_g. To compare the relaxation times of systems with different channel diameters, we define $\tau_g = 40.2$, by choosing the longest relaxation time accessible to all the systems we studied, then rescale the temperature of each system by the corresponding T_g [Fig. 15(a)]. With such a scaling, all the systems appear to have different fragilities. However, the FS crossover occurs at the same value of ϕ as the maximum in the C_p, for all channel diameters, which suggests there is an alternative scaling temperature. For each H_d, we locate the temperature of the C_p maximum $T_{\max}$, using our thermodynamic analysis, and define τ_0 as the relaxation time at $T_{\max}$. By rescaling the temperatures and relaxation times by $T_{\max}$ and τ_0, respectively, we find that all our data now collapse

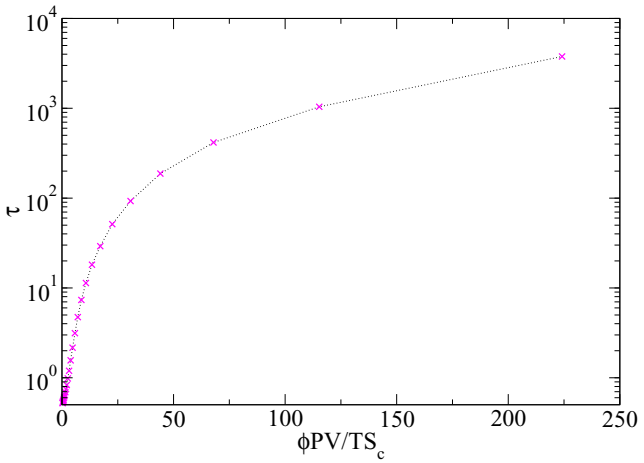

FIG. 16. (Color online) Adam-Gibbs plot for $H_d/\sigma = 1.866$.

onto a single master curve [see Fig. 15(b)]. This suggests that the temperature at the C_p maximum provides a more meaningful, and physically motivated, scaling temperature for our model than an arbitrarily selected glass transition transition temperature.

The FD model suggests that the fragile-strong crossover should be related to the concentration of excited regions. In our system, these excited regions can be identified as the defects because disks in the dense fluid regime can only move by hopping into the "vacancy" associated with a type 2 or type 4 local packing arrangements. At low ϕ, there is a high concentration of defects that can interact. When two defects are located next to each other, in a $-1-4-4-3-$ or $-3-2-2-1-$ arrangement, the local packing becomes unstable, which leads to directed, spontaneous, and irreversible particle motions that annihilate the defects to form the stable $-1-3-1-3-$ arrangement. This cooperative particle motion is characteristic of a fragile fluid. Once the defect concentration drops below a critical concentration, structural relaxation occurs through the directionally independent, activated hopping of particles located in isolated defects, which is characteristic of a strong fluid. In the strong fluid regime, $\ln\tau \sim \ln\theta$ which is confirmed in Fig. 15(c), at ϕ, above the C_p maximum.

Having been able to calculate the configurational entropy for our system exactly and measure the relaxation times, we are in a position to directly test the Adam-Gibbs relation for our model. A recent analysis [61,62] of the Adam-Gibbs relation, in terms of the random first order transition theory [63], suggests it has the general form

$$\ln\tau \sim \left(\frac{\phi PV}{TS_c}\right)^{\alpha}, \tag{27}$$

where the value of α is dependent on the dimensionality of the system. The usual form of the Adam-Gibbs relation for three dimensions is recovered with $\alpha = 1$. Unfortunately, we are unable to fit Eq. (27) to our data, over any region, and Fig. 16 shows our results for the standard Adam-Gibbs relation. This is consistent with the work of Sengupta *et al.* [61,62] who also found that the Adams-Gibbs relation did not work in two dimensions.

V. DISCUSSION

The potential energy landscape, and its hard particle equivalent, provide one of the main paradigms used to understand the properties of liquids, glasses, and jamming phenomena. However, the complexity of the landscape and the challenges associated with mapping configurations to their local inherent structures make it difficult to determine exactly how the thermodynamics and dynamics are related to the features of the landscape. This work develops a comprehensive picture of these relationships for a model where both the landscape and the inherent structure mapping can be determined exactly.

A distribution of jammed states implies the existence of a J line, as suggested by RMFT, rather than a particular J point, but there are a number of interesting features in the landscape that can be connected to thermodynamic and dynamic properties of the fluid. In RMFT, ϕ_d represents the occupied volume fraction where the fluid begins to be trapped in the basins of long lasting glassy states. Configurations at ϕ_d map to ϕ_{th}, which terminates the J line in the low ϕ_J limit. In our quasi-one-dimensional hard disk model, we identify ϕ_d as the ϕ where the saddle point index becomes very low and the dynamics becomes activated. Dynamically, this is consistent with RMFT and mode coupling theory (MCT). However, we find that the J line extends well below ϕ_{th}. The ideal gas maps to the jammed states with ϕ_J^*, at the maximum of S_J, which marks the lowest ϕ_J accessible to the equilibrium fluid. If the fluid did sample states below ϕ_J^* it would be unable to satisfy the maximum entropy condition for equilibrium because $\partial S_J/\partial\phi_J > 0$ [32]. The inherent structure pressure would also become negative, which is not possible in a hard particle system. From an operational perspective, the J point was originally defined as the ϕ_J of jammed structures quenched from the ideal gas configurations, which in the current system is ϕ_J^*. While the jammed states below ϕ_J^* are inaccessible from a thermodynamic standpoint, they may be formed through different compression protocols. Fluctuations in small systems will also allow these states to be observed. In general, the jamming phase diagram identified here looks similar to that proposed by Ciamarra *et al.* [5,64] for a granular system, but we have established clear connections between the landscape and the equilibrium fluid.

The thermodynamic functions C_p and P_{IS} both exhibit maxima as a function of ϕ that primarily result from the inflection in the S_c as the fluid moves toward the most dense state. The actual location of the maxima, and the inherent structure basins they are sampling, differ for each because the various thermodynamic functions are effected differently by the competition between the configurational and free volume contributions to the partition function. In particular, the coincidence between the location of the P_{IS} maximum and the $\phi_{J\,\mathrm{min}}$ appears fortuitous, rather than an indicator of a general thermodynamic relationship. For example, a binary system of nonadditive hard rods exhibits a similar inherent structure landscape [34], but the maxima in the C_p and P_{IS} both occur at ϕ well above $\phi_{J\,\mathrm{min}}$ [65], while the ideal gas configurations still map to the maximum in the distribution of the S_J.

Silica [66,67], silicon [68], and water [69–72] exhibit fragile-strong dynamical crossovers located at the C_p maximum associated with the Widom line while the KA BLJM

system has also been shown to exhibit an FS crossover at the mode coupling temperature [48]. Mallance *et al.* [73] recently suggested an FS-crossover temperature occurred in a broad range of glass forming liquids at temperatures below T_g. However, a subsequent analysis of some of the experimental data used in the Mallance *et al.* study showed that this was not the case [74]. Our model clearly exhibits an FS-crossover located at the C_p maximum as highlighted by both the curve fitting of a variety of different fragile behavior equations and by the derivative analysis shown in Fig. 14. Furthermore, we note that the temperature of the C_p maximum provides a better, physically motivated, rescaling of the structural relaxation times for the various channel diameters than does an arbitrarily defined T_g.

Defects play an integral role in the dynamics of this quasi-one-dimensional model and appear to establish a link between the dynamics and the thermodynamics, through the C_p maximum. In particular, neighboring defects are unstable and result in an irreversible local rearrangement of the particles, which appears to give rise to the super-Arrhenius dynamics of a fragile fluid. Once the defect concentration is low (the saddle point index is also low), the dynamics crosses over to the reversible hopping of defects between locally stable environment, which is characteristic of a strong fluid. Earlier studies of the instantaneous normal modes of the fragile and strong phase of silica [75] and the energy landscape of atomic clusters [76] have shown similar connections between saddle points, minima hopping, and the fragile-strong crossover. Simulations of bulk materials have also shown that local soft modes are spatially correlated with the highly mobile particles connected to dynamic heterogeneities [77–79].

The particle rearrangements associated with defects provide a comprehensive picture for the structural relaxation dynamics of the current quasi-one-dimensional hard disk model, but how important are defects to the question of structural relaxation in amorphous materials in general? Some systems with strong directional bonding interactions, such as silica and water, are capable of forming random tetrahedral networks (RTN) of bonds. Recent simulation studies [72] of the ST2 model of water [80] have shown that the FS crossover can be described in terms of the concentration of defects in the network, while similar results have been obtained for network forming colloids [81] and nanoparticles [82]. The structural relaxation of a two-dimensional random tiling model has also been described in terms of defect motion [83]. These studies suggest that understanding how defects effect structural relaxation may provide insight to the dynamics of amorphous systems.

As the local environments of the particles become less well defined, it becomes increasingly difficult to identify defects. For example, in the hard disks model considered here, the extreme confinement induces structure and ensures there are only four local packing environments. When the channel diameter increases beyond $H_d/\sigma = 1.866$, the disks can also contact their second nearest neighbors which increases the number of local environments to 32 [33]. Nevertheless, the concept of incompatibility between local environments remains. Some local particle arrangements cannot be combined to form a stable jammed structure and we would expect the particles to spontaneously rearrange to form a more stable state.

ACKNOWLEDGMENTS

We would like to thank Natural Sciences and Engineering Council of Canada for financial support. We also thank WestGrid and Compute Canada for providing computational resources. R.K.B. thanks M. A. Moore for helpful discussions. S.S.A. would like to thank K. Miyazaki for fruitful discussions.

[1] J. D. Bernal and J. Mason, Nature (London) **188**, 910 (1960).
[2] *Unifying Concepts in Granular Media and Glasses: From the Statistical Mechanics of Granular Media to the Theory of Jamming*, edited by A. Coniglio, A. Fierro, H. J. Herrmann, and M. Nicodem (Elsevier, Amsterdam, 2004).
[3] M. van Hecke, J. Phys.: Condens Matter **22**, 033101 (2009).
[4] S. Torquato and F. H. Stillinger, Rev. Mod. Phys. **82**, 2633 (2010). .
[5] M. Pica Ciamarra, A. Coniglio, and A. De Candia, Soft Matter **6**, 2975 (2010).
[6] A. J. Liu and S. R. Nagel, Nature (London) **396**, 21 (1998).
[7] C. S. O'Hern, S. A. Langer, A. J. Liu, and S. R. Nagel, Phys. Rev. Lett. **88**, 075507 (2002).
[8] C. S. O'Hern, L. E. Silbert, A. J. Liu, and S. R. Nagel, Phys. Rev. E **68**, 011306 (2003).
[9] T. K. Haxton, M. Schmiedeberg, and A. J. Liu, Phys. Rev. E **83**, 031503 (2011).
[10] M. Mezard and A. Montanari, *Information, Physics, and Computation* (Oxford University Press, Oxford, UK, 2009).
[11] C. A. Rogers, *Packing and Covering* (Cambridge University Press Cambridge, Cambridge, 1964).
[12] M. Goldstein, J. Chem. Phys. **51**, 3728 (1969).
[13] F. H. Stillinger, E. A. DiMarzio, and R. L. Kornegay, J. Chem. Phys. **40**, 1564 (1964).
[14] F. H. Stillinger and T. A. Weber, Phys. Rev. A **25**, 978 (1982).
[15] S. Torquato and F. H. Stillinger, J. Phys. Chem. B **105**, 11849 (2001).
[16] P. G. Debenedetti, *Metastable Liquids. Concepts and Principles* (Princeton University Press, Princeton, NJ, 1996).
[17] P. G. Debenedetti and F. H. Stillinger, Nature (London) **410**, 259 (2001).
[18] G. Adam and J. H. Gibbs, J. Chem. Phys. **43**, 139 (1965).
[19] R. J. Speedy, J. Chem. Phys. **114**, 9069 (2001).
[20] N. Xu, J. Blawzdziewicz, and C. S. O'Hern, Phys. Rev. E **71**, 061306 (2005).
[21] A. Donev, F. H. Stillinger, and S. Torquato, Phys. Rev. Lett. **96**, 225502 (2006).
[22] A. V. Anikeenko, N. N. Medvedev, and T. Aste, Phys. Rev. E **77**, 031101 (2008).
[23] S. Torquato, T. M. Truskett, and P. G. Debenedetti, Phys. Rev. Lett. **84**, 2064 (2000).
[24] G. Parisi and F. Zamponi, J. Chem. Phys. **123**, 144501 (2005).
[25] G. Parisi and F. Zamponi, Rev. Mod. Phys. **82**, 789 (2010).

[26] P. Chaudhuri, L. Berthier, and S. Sastry, Phys. Rev. Lett. **104**, 165701 (2010).
[27] C. F. Schreck, C. S. O'Hern, and L. E. Silbert, Phys. Rev. E **84**, 011305 (2011).
[28] M. Ozawa, T. Kuroiwa, A. Ikeda, and K. Miyazaki, Phys. Rev. Lett. **109**, 205701 (2012).
[29] M. Clusel, E. I. Corwin, A. O. N. Siemens, and J. Brujić, Nature (London) **460**, 611 (2009).
[30] Y. Jin, J. G. Puckett, and H. A. Makse, Phys. Rev. E **89**, 052207 (2014).
[31] M. Z. Yamchi, S. S. Ashwin, and R. K. Bowles, Phys. Rev. Lett. **109**, 225701 (2012).
[32] S. S. Ashwin, M. Zaeifi Yamchi, and R. K. Bowles, Phys. Rev. Lett. **110**, 145701 (2013).
[33] S. S. Ashwin and R. K. Bowles, Phys. Rev. Lett. **102**, 235701 (2009).
[34] R. K. Bowles, Phys. A (Amsterdam) **275**, 217 (2000).
[35] R. K. Bowles and I. Saika-Voivod, Phys. Rev. E **73**, 011503 (2006).
[36] S. F. Edwards and D. V. Grinev, Phys. Rev. E **58**, 4758 (1998).
[37] R. K. Bowles and S. S. Ashwin, Phys. Rev. E **83**, 031302 (2011).
[38] R. M. Irastorza, C. M. Carlevaro, and L. A. Pugnaloni, J. Stat. Mech. (2013) P12012.
[39] N. Gundlach, M. Karbach, D. Liu, and G. Muller, J Stat. Mech. (2013) P04018.
[40] C. Moore, D. Liu, B. Ballnus, M. Karbach, and G. Muller, J Stat Mech. (2014) P04008.
[41] J. A. Barker, Aust. J. Phys. **15**, 127 (1962).
[42] D. H. Kofke and A. J. Post, J. Chem. Phys. **98**, 4853 (1993).
[43] F. Sciortino and P. Tartaglia, Phys. Rev. Lett. **78**, 2385 (1997).
[44] C. Donati, F. Sciortino, and P. Tartaglia, Phys. Rev. Lett. **85**, 1464 (2000).
[45] L. Angelani, R. Di Leonardo, G. Ruocco, A. Scala, and F. Sciortino, Phys. Rev. Lett. **85**, 5356 (2000).
[46] K. Broderix, K. K. Bhattacharya, A. Cavagna, A. Zippelius, and I. Giardina, Phys. Rev. Lett. **85**, 5360 (2000).
[47] W. Kob and H. C. Andersen, Phys. Rev. E **51**, 4626 (1995).
[48] S. S. Ashwin and S. Sastry, J Phys.: Condens. Matter **15**, S1253 (2003).
[49] M. J. Godfrey and M. A. Moore, Phys. Rev. E **89**, 032111 (2014).
[50] M. S. Shell, P. G. Debenedetti, E. La Nave, and F. Sciortino, J. Chem. Phys. **118**, 8821 (2003).
[51] B. D. Lubachevsky and F. H. Stillinger, J. Stat. Phys. **60**, 561 (1990).
[52] S. Varga, G. Balló, and P. Gurin, J. Stat. Mech. (2011) P11006.
[53] P. Gurin and S. Varga, J. Chem. Phys. **139**, 244708 (2013).
[54] H. Vogel, Phys. Z. **22**, 645 (1921).
[55] G. S. Fulcher, J. Am. Ceram. Soc. **8**, 339 (1925).
[56] G. Tammany and W. Hesse, Z. Anorg. Allg. Chem. **156**, 245 (1926).
[57] Y. S. Elmatad, D. Chandler, and J. P. Garrahan, J. Phys. Chem. B **113**, 5563 (2009).
[58] Y. S. Elmatad, D. Chandler, and J. P. Garrahan, J. Phys. Chem. B **114**, 17113 (2010).
[59] J. P. Garrahan and D. Chandler, Proc. Natl. Acad. Sci. USA **100**, 9710 (2003).
[60] C. A. Angell, J. Non-Cryst. Solids **131**, 13 (1991).
[61] S. Sengupta, S. Karmakar, C. Dasgupta, and S. Sastry, Phys. Rev. Lett. **109**, 095705 (2012).
[62] S. Sengupta, S. Karmakar, C. Dasgupta, and S. Sastry, J. Chem. Phys. **138**, 12A548 (2013).
[63] T. R. Kirkpatrick, D. Thirumalai, and P. G. Wolynes, Phys. Rev. A **40**, 1045 (1989).
[64] M. P. Ciamarra and A. Coniglio, Phys. Rev. Lett. **101**, 128001 (2008).
[65] M. Z. Yamchi, Ph.D. thesis, *The Packing Landscape of Quasi–One Dimensional Hard Sphere Systems*, University of Saskatchewan, 2014.
[66] I. Saika-Voivod, P. Poole, and F. Sciortino, Nature (London) **412**, 514 (2001).
[67] I. Saika-Voivod, F. Sciortino, and P. H. Poole, Phys. Rev. E **69**, 041503 (2004).
[68] S. Sastry and C. A. Angell, Nat. Mater. **2**, 739 (2003).
[69] L. Xu, P. Kumar, S. V. Buldyrev, S. H. Chen, P. H. Poole, F. Sciortino, and H. E. Stanley, Proc. Natl. Acad. Sci. USA **102**, 16558 (2005).
[70] H. E. Stanley, P. Kumar, G. Franzese, L. Xu, Z. Yan, M. G. Mazza, S. V. Buldyrev, S. H. Chen, and F. Mallamace, Eur. Phys. J., Spec. Top. **161**, 1 (2008).
[71] C. A. Angell, Science **319**, 582 (2008).
[72] P. H. Poole, S. R. Becker, F. Sciortino, and F. W. Starr, J. Phys. Chem. B **115**, 14176 (2011). .
[73] F. Mallamace, C. Branca, C. Corsaro, N. Leone, J. Spooren, S.-H. Chen, and H. E. Stanley, Proc. Natl. Acad. Sci. USA **107**, 22457 (2010).
[74] Z. Chen, C. A. Angell, and R. Richert, Eur. Phys. J. E **35**, 65 (2012).
[75] E. La Nave, H. E. Stanley, and F. Sciortino, Phys. Rev. Lett. **88**, 035501 (2002).
[76] S. Banerjee and C. Dasgupta, Phys. Rev. E **85**, 021501 (2012).
[77] A. Widmer-Cooper, H. Perry, P. Harrowell, and D. R. Reichman, Nat. Phys. **4**, 711 (2008).
[78] A. Widmer-Cooper and P. Harrowell, Phys. Rev. E **80**, 061501 (2009).
[79] M. D. Ediger and P. Harrowell, J. Chem. Phys. **137**, 080901 (2012).
[80] F. H. Stillinger and A. Rahman, J. Chem. Phys. **60**, 1545 (1974).
[81] C. De Michele, S. Gabrielli, P. Tartaglia, and F. Sciortino, J. Phys. Chem. B **110**, 8064 (2006).
[82] F. W. Starr and F. Sciortino, J. Phys.: Condens Matter **18**, L347 (2006).
[83] E. Tondl, M. Ramsay, P. Harrowell, and A. Widmer-Cooper, J. Chem. Phys. **140**, 104503 (2014).